

NW Pacific-Panthalassa intra-oceanic subduction during Mesozoic times from mantle convection and geoid models

Yi-An Lin¹, Lorenzo Colli¹, and Jonny Wu¹

¹University of Houston

November 24, 2022

Abstract

Pacific-Panthalassa plate tectonics back to Jurassic times are recognized as the most challenging on Earth to reconstruct, due partly to a large (>9000 km length) unconstrained area between the Pacific and Laurasia (now NE Asia) during the Early Jurassic. We built four contrasted NW Pacific-Panthalassa global plate reconstructions and assimilated their velocity fields into global geodynamic models. We compare our predicted mantle structure, synthetic geoid and dynamic topography to Earth observations. P-wave tomographic filtering of predicted mantle structures allowed for more explicit comparisons to global tomography. Plate reconstructions that include intra-oceanic subduction in NW Pacific-Panthalassa fit better to the observed geoid and residual topography, challenging the Andean-style subduction along East Asia. Our geodynamic models predict significant SE-ward lateral slab advections within the NW Pacific basin lower mantle (~2500 km from Mesozoic times to present), which can confound “vertical slab sinking”-style restorations of past subduction zone locations.

1 **NW Pacific-Panthalassa intra-oceanic subduction during Mesozoic times from**
2 **mantle convection and geoid models**

3

4 Yi-An Lin^{1,*}, Lorenzo Colli¹, Jonny Wu^{1,*}

5 ¹University of Houston, TX; *Corresponding author

6

7 **Abstract**

8

9 Pacific-Panthalassa plate tectonics back to Jurassic times are recognized as the most
10 challenging on Earth to reconstruct, due partly to a large (>9000 km length)
11 unconstrained area between the Pacific and Laurasia (now NE Asia) during the Early
12 Jurassic. We built four contrasted NW Pacific-Panthalassa global plate reconstructions
13 and assimilated their velocity fields into global geodynamic models. We compare our
14 predicted mantle structure, synthetic geoid and dynamic topography to Earth
15 observations. P-wave tomographic filtering of predicted mantle structures allowed for
16 more explicit comparisons to global tomography. Plate reconstructions that include
17 intra-oceanic subduction in NW Pacific-Panthalassa fit better to the observed geoid and
18 residual topography, challenging the Andean-style subduction along East Asia. Our
19 geodynamic models predict significant SE-ward lateral slab advections within the NW
20 Pacific basin lower mantle (~2500 km from Mesozoic times to present), which can
21 confound 'vertical slab sinking'-style restorations of past subduction zone locations.

22

23

24

25 **1. Introduction**

26

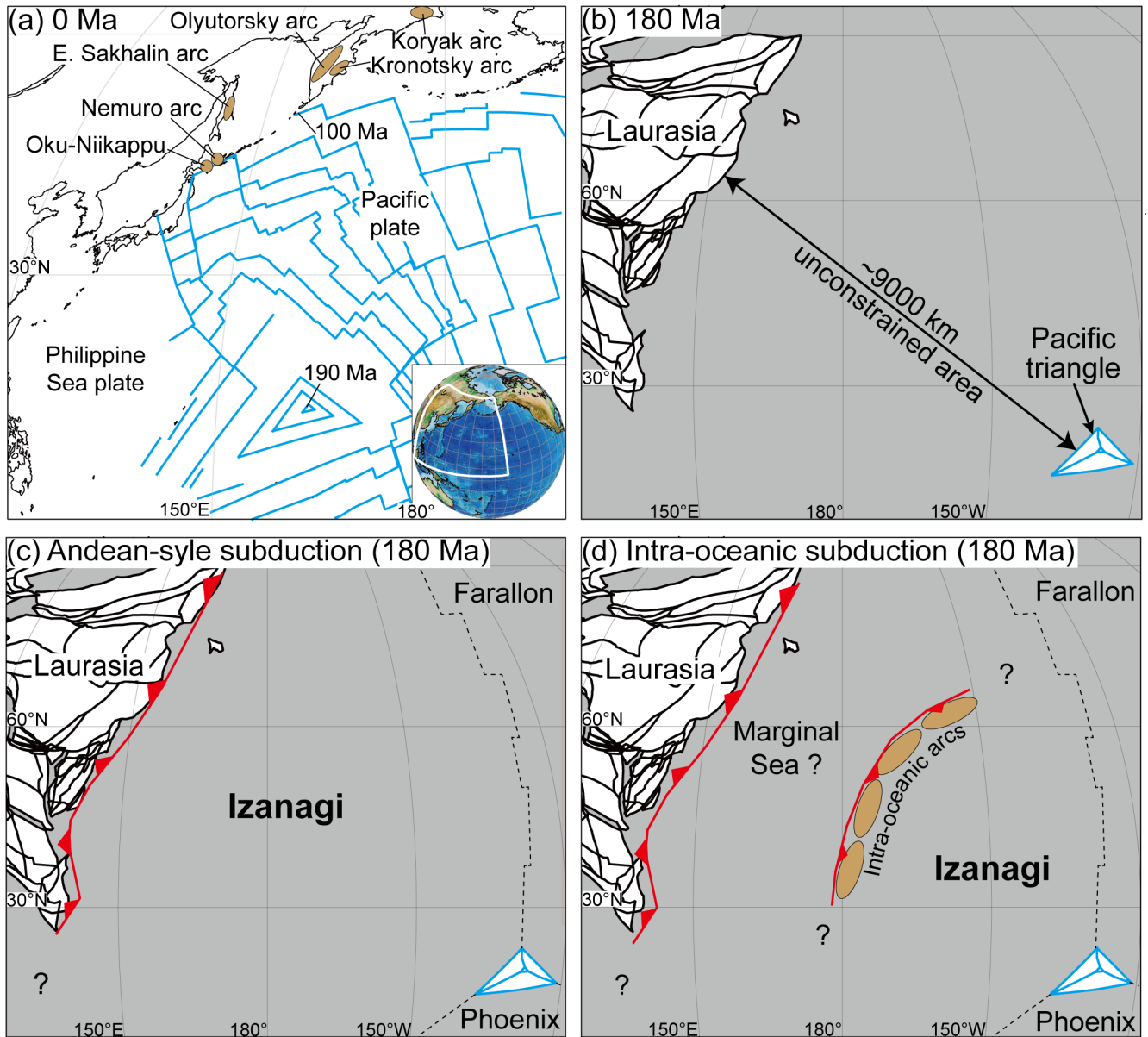
27 Within Earth's tectonic history during the Mesozoic and Cenozoic eras, the evolution of
28 the Pacific Ocean and its predecessor ocean, Panthalassa, is the most challenging to
29 reconstruct (Müller et al., 2016). The Pacific Ocean currently covers >25% of the
30 present Earth surface and is the largest ocean basin on Earth; but it was even larger
31 during the late Mesozoic, when the Pacific-Panthalassa oceanic realm covered ~45% of
32 Earth (Torsvik et al., 2019). This shrinking of the Pacific-Panthalassa realm since the
33 Mesozoic has been accommodated by subduction. Lost Pacific-Panthalassa oceanic
34 lithosphere is one of the most significant contributors to global plate tectonic uncertainty
35 (Torsvik et al., 2019). This paper discusses the plate tectonic history of NW Pacific-
36 Panthalassa and its implications for subduction histories and accreted oceanic terranes
37 along East Asia (Fig. 1a) using forward geodynamic models to assimilate contrasted
38 NW Pacific-Panthalassa plate reconstructions and explicitly test them against mantle
39 structure, the geoid and dynamic topography.

40

41 Seafloor magnetic lineations indicate that the oldest Pacific plate is a triangle-shaped
42 area with ages ~190 Ma (Wright et al., 2016), known as the 'Pacific triangle' (Figs. 1a,
43 b). Pacific-Panthalassa plate reconstructions back to Jurassic times show that only the
44 Pacific triangle has been preserved, with the adjacent oceanic lithosphere (>90% of the
45 total area) now completely subducted and lost (grey areas in Fig. 1b). Within the NW
46 Pacific-Panthalassa, global reconstructions indicate a >9000 km length of unconstrained

47 area between the Pacific triangle and Laurasia (now NE Asia) during the Early Jurassic
48 (Fig. 1b). The Pacific triangle magnetic lineations imply the Pacific plate grew from the
49 spreading of three connected ridges, whose conjugate rift flanks were named Izanagi,
50 Phoenix, and Farallon. Except for remnants of the Farallon plate, these conjugate plates
51 are completely subducted. Their spatial extent and evolution back in time are thus very
52 uncertain. A simple and straightforward hypothesis is mirroring and interpolating the NW
53 Pacific plate magnetic anomalies to create synthetic seafloor isochrons (e.g. Müller et
54 al., 2016), allowing fully-kinematic, globally-consistent plate histories to be modeled for
55 the Izanagi plate; however, actual details remain poorly known and are briefly reviewed
56 below.

57



58
 59 Figure 1. (a) Present-day isochrons (blue lines) of the Pacific plate from Müller et al.
 60 (2016) and accreted terranes on the NE Asian continent (in text). (b) Plate
 61 reconstruction of western Pacific Ocean during Jurassic time shows ~9000 km
 62 unconstrained area between Jurassic Pacific plate and Eurasia. The Pacific triangle is
 63 the earliest formed part of the Pacific plate. (c) Reconstructed Andean-style subduction
 64 along Laurasia during the Jurassic (Müller et al., 2016), in contrast to (d) intra-oceanic
 65 subduction within Pacific-Panthalassa (e.g. van der Meer et al., 2012).
 66

67 *1.1 Plate tectonic reconstructions of the NW Pacific Ocean basin*

69 'Andean-style' plate tectonic reconstructions indicate the size and motion of the Pacific
70 and Izanagi plates by attributing all Pacific-Panthalassa-Eurasian convergence (>9000
71 km since the Jurassic) to subduction along the Eurasian margin; no intra-oceanic
72 subduction occurred within NW Pacific-Panthalassa (Fig. 1c). These assumptions imply
73 a large, long-lived Izanagi plate extending from central Panthalassa to the Eurasian
74 margin and converging continually towards Eurasia (Fig. 1c) (e.g. Engebretson et al.,
75 1984; Müller et al., 2016; Seton et al., 2012; Whittaker et al., 2007). To date, almost all
76 published geodynamic models implement Andean-style plate reconstructions for the
77 NW Pacific (e.g. Flament, 2018; Lin et al., 2020; Matthews et al., 2016).

78

79 In contrast, a second class of 'intra-oceanic subduction' plate reconstructions imply
80 intra-oceanic arcs within Pacific-Panthalassa (Fig. 1d). These plate reconstructions are
81 based on accreted Mesozoic-aged intra-oceanic arcs along East Asia (brown polygons
82 in Fig. 1a) and supported by fast, slab-like anomalies in mantle tomographic images
83 under the present Pacific or near the East Asian margin (e.g. Domeier et al., 2017;
84 Ueda & Miyashita, 2005; van der Meer et al., 2012; Yamasaki & Nanayama, 2018).
85 Island arcs apparently accreted along easternmost Eurasia during the earliest
86 Cretaceous ~145 Ma at NE Japan (Ueda & Miyashita, 2005), along the Russian Far
87 East during the mid-Cretaceous (Filatova & Vishnevskaya, 1997); and along Hokkaido,
88 Kamchatka, and East Sakhalin during the Late Cretaceous to the mid-Eocene (Alexeiev
89 et al., 2006; Konstantinovskaia, 2000; Nokleberg, 2010; Shapiro & Solov'ev, 2009;
90 Zharov, 2005).

91

92 Some plate reconstructions that explain these accreted island arcs imply the existence
93 of NW Pacific-Panthalassa intra-oceanic subduction zones and additional plates other
94 than Izanagi (Fig. 1d) (e.g. Domeier et al., 2017; Vaes et al., 2019; van der Meer et al.,
95 2012). However, other studies explain the Japan accretionary complexes by a >1000
96 km northwards translation from South China or Tethys by sinistral strike-slip along the
97 eastern Eurasian margin within an Andean-style NW Pacific plate tectonic context (e.g.
98 Fujisaki et al., 2014; Sakashima et al., 2003). Only limited attempts (e.g. Seton et al.,
99 2018) have been made to test the viability of intra-oceanic subduction within the NW
100 Pacific using global geodynamic models due, in part, to the challenges of building plate
101 reconstructions with limited constraints (e.g. Fig. 1b). In this study, we approach this
102 challenge by creating a series of increasingly complex plate reconstructions featuring
103 intra-oceanic subduction in the NW Pacific-Panthalassa. We then assimilate them into
104 global geodynamic models and probe for improved fits to imaged mantle structure and
105 Earth's geoid. We discuss implications for plate tectonics, the history of mantle flow, and
106 NE Asian dynamic topography.

107

108 **2. Method**

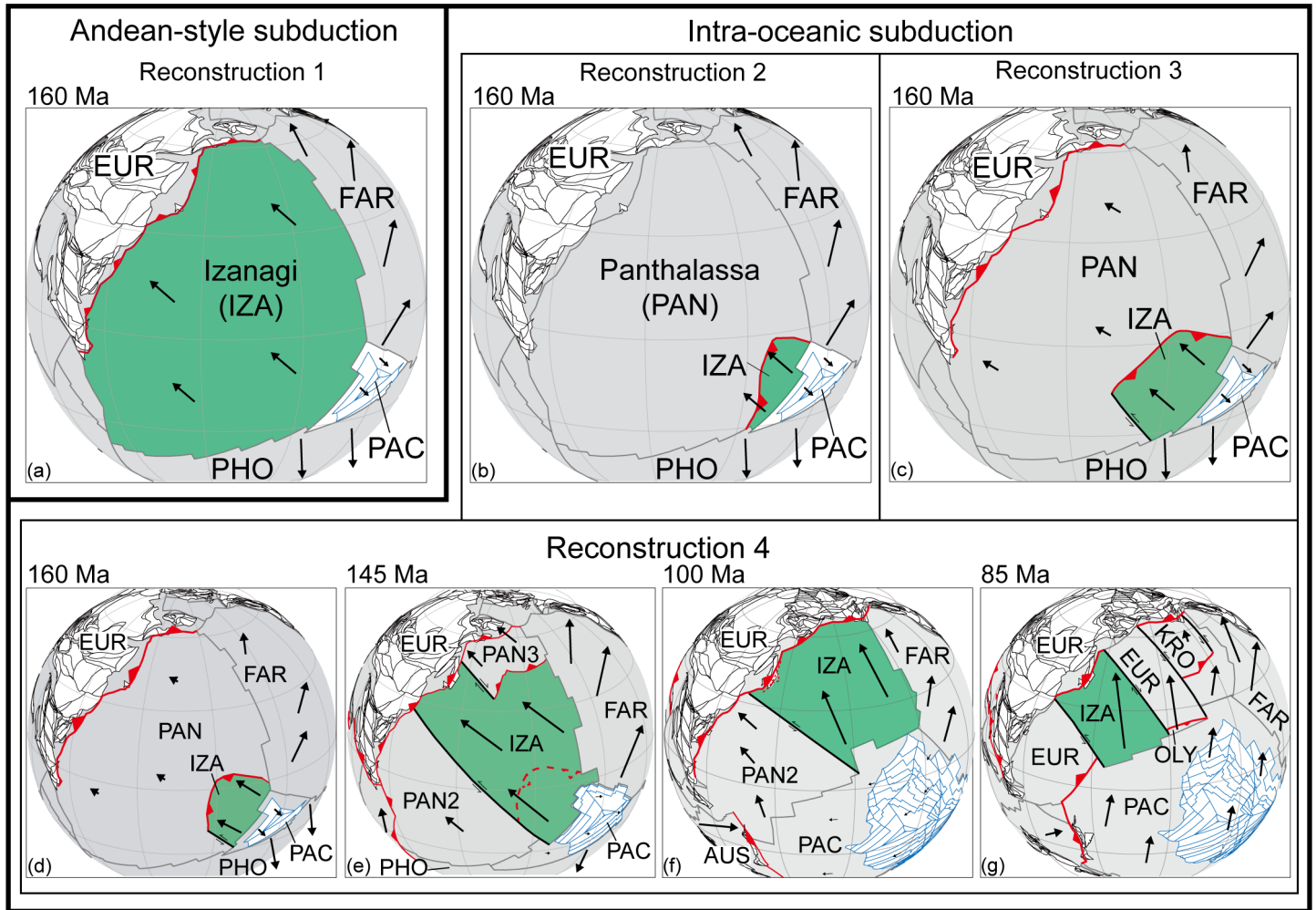
109

110 Mantle circulation models use global plate velocities as input in the form of time-
111 dependent boundary conditions to link surface processes and the deep Earth (e.g.
112 Bunge & Grand, 2000; Nerlich et al., 2016; Zahirovic et al., 2016). Previous geodynamic
113 studies that addressed NW Pacific plate tectonics typically rely on assimilation of a
114 single input plate tectonic reconstruction while testing other parameter spaces (e.g.

115 viscosity) (Cao et al., 2018; Seton et al., 2015). Here we take a different approach from
116 previous studies and assimilate four contrasted global plate reconstructions within three
117 whole-mantle viscosity profiles (Cases a to c. See Fig. S2; Table S1), for a total of
118 twelve geodynamic models. Three of the four global plate reconstructions are built
119 specifically for this study (see Supplemental for details). Our fourth plate reconstruction
120 was previously published (Matthews et al., 2016) and is our reference model.

121

122 We test two end-member classes of plate reconstructions that we call ‘Andean-style’
123 and ‘intra-oceanic’ subduction (Figs. 2, S1). *Andean-style subduction* of the Izanagi
124 (IZA) plate along the Eurasian continental margin is assimilated from a global
125 reconstruction from 460 to 0 Ma based on Matthews et al. (2016) (Figs. S1a-e), which is
126 called ‘Reconstruction 1’. In this model, all western Pacific-Eurasia plate convergence
127 after the Jurassic is consumed by a single subduction zone along the eastern Eurasian
128 margin (Movie 1). This reconstruction results in the largest IZA plate relative to the other
129 reconstructions (Fig. 2a). *Intra-oceanic subduction* within the western Pacific Ocean is
130 featured by ‘Reconstructions 2, 3 and 4’ (Fig. 2). Various intra-oceanic subduction-style
131 plate reconstructions for the western Pacific Ocean have been proposed due to sparse
132 geological and kinematic constraints (e.g. Fig. 1). As such, we built a suite of three plate
133 reconstructions with increasing complexity based on published regional plate
134 reconstructions (Movies 2 to 4). They all follow the Andean-style Reconstruction 1 from
135 460 Ma until Jurassic times (at 160, 180, or 190 Ma; Table S2) and then implement
136 alternative plate kinematic histories during mid-Mesozoic to early Cenozoic times (see
137 Supplemental for details).



Subduction zones
 Extinct arcs
 Strike slip faults
 Existing Pacific seafloor
 Plate boundaries

1: Plate motions relative to EUR

139 Figure 2. Representative maps showing the four main plate reconstructions assimilated
 140 into the geodynamic models in this study. (a) Andean-style subduction (Reconstruction
 141 1) is the default model from Matthews et al. (2016). (b)-(g) Reconstructions 2 to 4
 142 implemented intra-oceanic subduction in western Pacific Ocean. (b) Reconstruction 2
 143 implemented a size-limited Izanagi plate (IZA) overriding Panthalassa plate (PAN),
 144 which is stationary relative to Eurasia (EUR). (c) Reconstruction 3 implemented intra-
 145 oceanic subduction of IZA during 180-145 Ma while keeping the Eurasian margin active
 146 (although at a reduced convergence rate with respect to Reconstruction 1), followed by
 147 Andean style subduction after 145 Ma. (d)-(g) Reconstruction 4 builds upon
 148 Reconstruction 3 and accounts for the terrane accretion at Kamchatka, magmatic
 149 records along Eurasia and recently published NE Asia plate reconstructions (e.g. Vaes
 150 et al., 2019). PAC: Pacific plate; FAR: Farallon plate; PHO: Phoenix plate; IND: Indian
 151 plate; AUS: Australia plate; PAN: Panthalassa plate; KUL: Kula plate; KRO: Kronotsky
 152 plate; OLY: Olyutorsky plate; PAN2: Panthalassa plate 2; PAN3: Panthalassa plate 3.
 153

154 **3. Results**

155

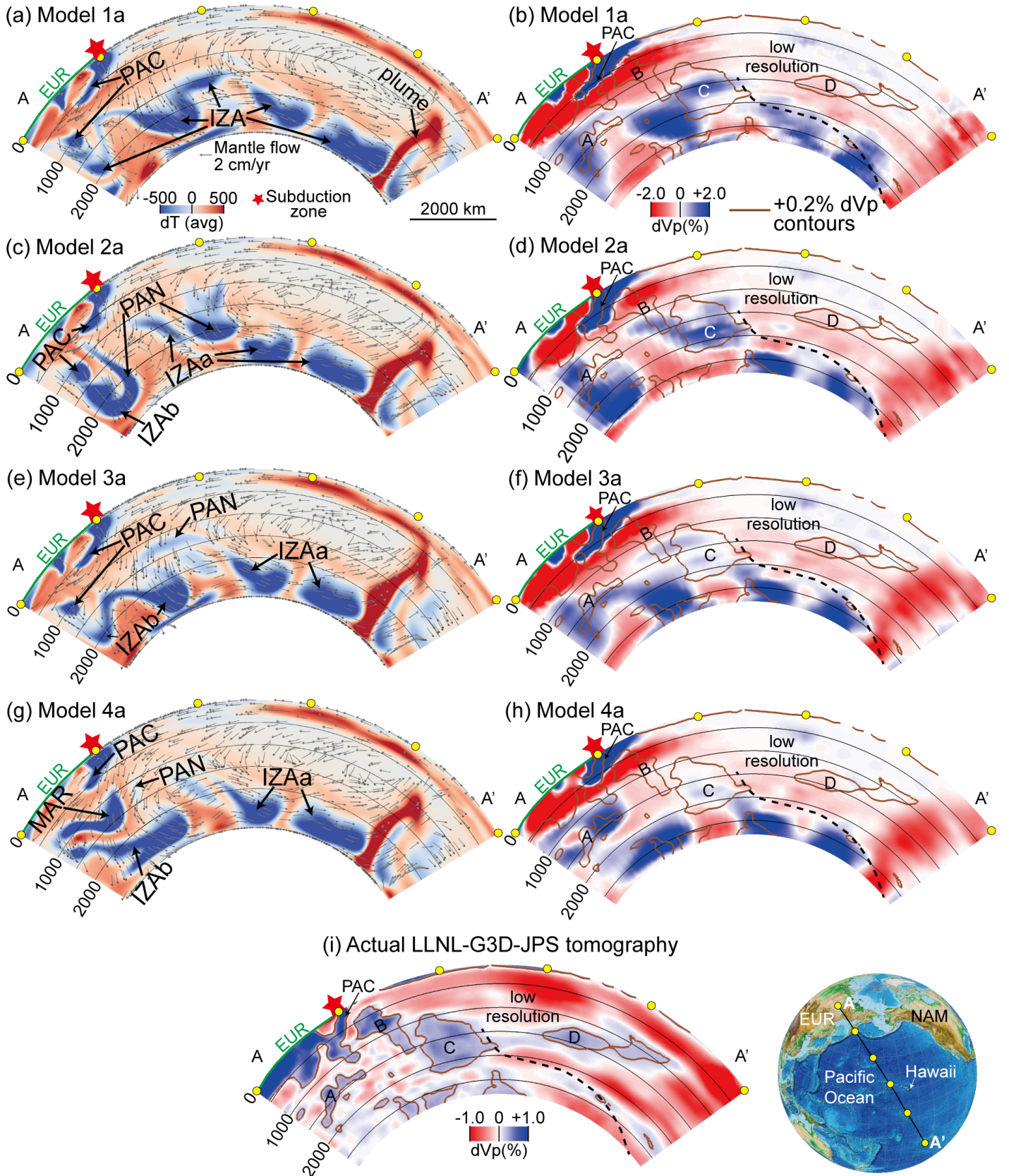
156 *3.1 Predicted and imaged mantle structure*

157

158 A cross-section A-A' across East Asia and the NW Pacific shows the present-day
159 mantle thermal structure and flow fields (Fig. 3 left column) predicted by geodynamic
160 Models 1a to 4a (i.e. Reconstructions 1 to 4 within geodynamic Case a, our preferred
161 viscosity profile; alternative viscosity profile Cases b and c are shown in Supplemental).
162 Despite significant variations in assimilated plate reconstructions (Fig. 2), all models
163 display relatively similar first-order mantle structures and flows (Fig. 3 left column) that
164 are characterized by: (1) shallower, stagnant Pacific slabs under the Eurasian margin
165 around 500 km depths; (2) large swaths of slab anomalies under or offshore from the
166 Eurasian margin entrained by downwelling flows; and, (3) slabs within the lowermost
167 lower mantle (>2000 km depths) under the central Pacific entrained in SE-directed flows
168 towards a plume within the central Pacific. In all models, the time-dependent mantle
169 evolution since the Late Jurassic shows SE-directed lower mantle 'return flows' towards
170 a plume in the central Pacific (Figs. S6, S7). These flows help to explain the relatively
171 similar mantle structures in Models 1a to 4a (Fig. 3) because the lower mantle return
172 flows advect all subducted slabs laterally towards the southeast (Figs. S6, S7). The
173 most extreme case is the Andean-style Model 1a, where Pacific-Panthalassa
174 subduction is continuously pinned to the Eurasian margin but the subducted slabs are
175 advected laterally within the lower mantle into the central Pacific by >2000 km since
176 Jurassic (Figs. 3, S6).

Full-resolution thermal structure

LLNL-G3D filtered seismic structure



178 Figure 3. Cross sections of the geodynamically modeled present-day mantle structure
179 for Model 1a to 4a. The left column shows the full-resolution thermal structure while the
180 right column shows the tomographically-filtered seismic structure. (a) Model 1a
181 produces extensive IZA slabs in the lower mantle beneath Eurasia and NW Pacific and
182 PAC slabs at upper 1000 km depths beneath Eurasian margin; (c) Model 2a produces
183 PAN slabs at 1000-2000 km depths, IZAa to the east of PAN slabs and IZAb to the west
184 of PAN slabs in the lower mantle; (e) Model 3a and (g) Model 4a produce IZAa in the
185 lower mantle to the east of IZAb, and (g) Model 4a produces MAR slabs at ~700-1600
186 km depths beneath Eurasia. LLNL-G3D filtered dVp for (b) Model 1a, (d) Model 2a, (f)
187 Model 3a, and (h) Model 4a are compared to (i) LLNL-G3D-JPS (Simmons et al., 2015)
188 seismic tomography. Izanagi slabs-a (IZAa) and Izanagi slabs-b (IZAb) are used to
189 differentiate the Izanagi subduction before and after 160 Ma. MAR: Marginal sea slabs
190 formed by closing NE Eurasian backarc basin. Brown lines in (b), (d), (f) and (h) show
191 +0.2% dVp contours from (i).
192

193 The right column of Figure 3 shows ‘synthetic tomography’ images of Models 1a to 4a
194 produced by converting the left-column temperature anomalies to seismic anomalies
195 using a thermodynamically self-consistent model of mantle mineralogy (Chust et al.,
196 2017; Stixrude & Lithgow-Bertelloni, 2011) and subsequently filtered with the LLNL-
197 G3D-JPS resolution operator (Simmons et al., 2019). After tomographic-filtering, the
198 shallow Pacific (PAC) slabs are still relatively well-imaged whereas the lower mantle
199 slabs (Fig. 3 right column) show more blurring relative to the full-resolution models.
200 LLNL-G3D-JPS seismic tomography (Simmons et al., 2015) shows the shallow PAC
201 slabs and four swaths of lower mantle fast anomalies A to D (Fig. 3i). We exclude fast
202 anomaly D from comparison due their occurrence within a recognized low resolution
203 region in the central Pacific (van der Meer et al., 2012). However, after tomographic
204 filtering, it is difficult to visually distinguish which predicted mantle state best fits actual
205 tomography (Fig. 3). Comparisons of tomographically-filtered horizontal slices at various
206 lower mantle depths within the NW Pacific basin show similar conclusions (Fig. S15).
207 Computed correlations for Models 1a to 4a and LLNL-G3D-JPS seismic tomography of

208 ~0.04-0.05 confirm that no single model shows a superior fit to tomography. Thus, we
209 conclude from the tomographic blurring produced by our tomographic filtering (e.g. Figs.
210 3, S15) that predicted and imaged mantle structure comparisons within the central
211 Pacific are likely hindered by limited tomographic resolution.

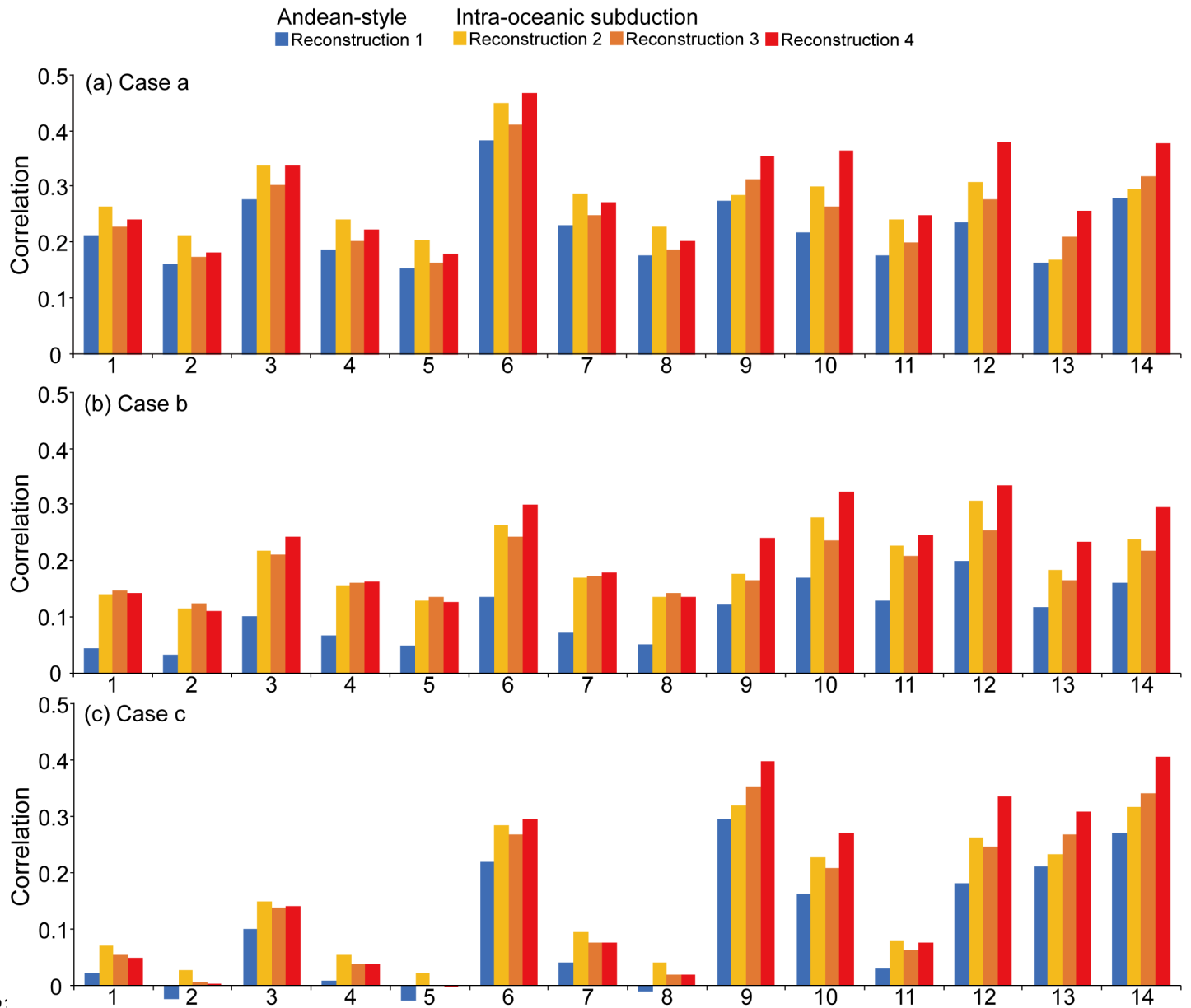
212

213 *3.2 Comparison between synthetic and observed geoid*

214

215 For each modeled present-day mantle structure we followed Thoraval and Richards
216 (1997) and computed the synthetic geoid and its correlation to the observed geoid (Fig.
217 4). The geoid response is sensitive to density and viscosity structure. As the forward
218 geoid problem is less computationally demanding, for each plate reconstruction we
219 computed 42 synthetic geoid responses employing a total of 14 viscosity profiles,
220 exploring a range of more extreme viscous layering scenarios (Fig. S3) for
221 geodynamically-derived mantle structures in 3 Cases (Fig. 4). Correlations range from
222 0.47 (viscosity profile 6 in Case a) to slightly negative, with an average correlation of
223 around 0.25 (Fig. 4), which is on par with a previous study (e.g. Flament, 2018). Despite
224 correlation variability between synthetic geoid, the Andean-style Reconstruction 1
225 produces the least satisfactory correlation in all cases (compare blue and reddish color
226 in Fig. 4). Within the better fitting intra-oceanic Reconstructions 2 to 4, Reconstruction 4
227 shows the best correlation in the majority of cases (23/42 in Fig. 4) whereas
228 Reconstruction 2 is superior in about one-third (13/42 in Fig. 4). Therefore, we choose
229 Reconstruction 4 as our preferred intra-oceanic reconstruction for the next section,
230 while acknowledging that no intra-oceanic reconstruction discussed here is universally-

231 superior. Regardless, our analysis indicates that as a plate reconstruction class, the
 232 intra-oceanic Reconstructions 2 to 4 are distinctively superior to the Andean-style
 233 Reconstruction 1 on the basis of predicted and observed geoid.
 234



236 Figure 4. Correlation between observed non-hydrostatic geoid and synthetic geoid from
 237 the present-day structures predicted by Reconstructions 1 to 4 for (a) Case a, (b) Case
 238 b and (c) Case c with various radial viscosity profiles 1 to 14. In all combinations, intra-
 239 oceanic Reconstructions 2 to 4 achieved higher correlations to the observed geoid
 240 relative to the Andean-style Reconstruction 1.

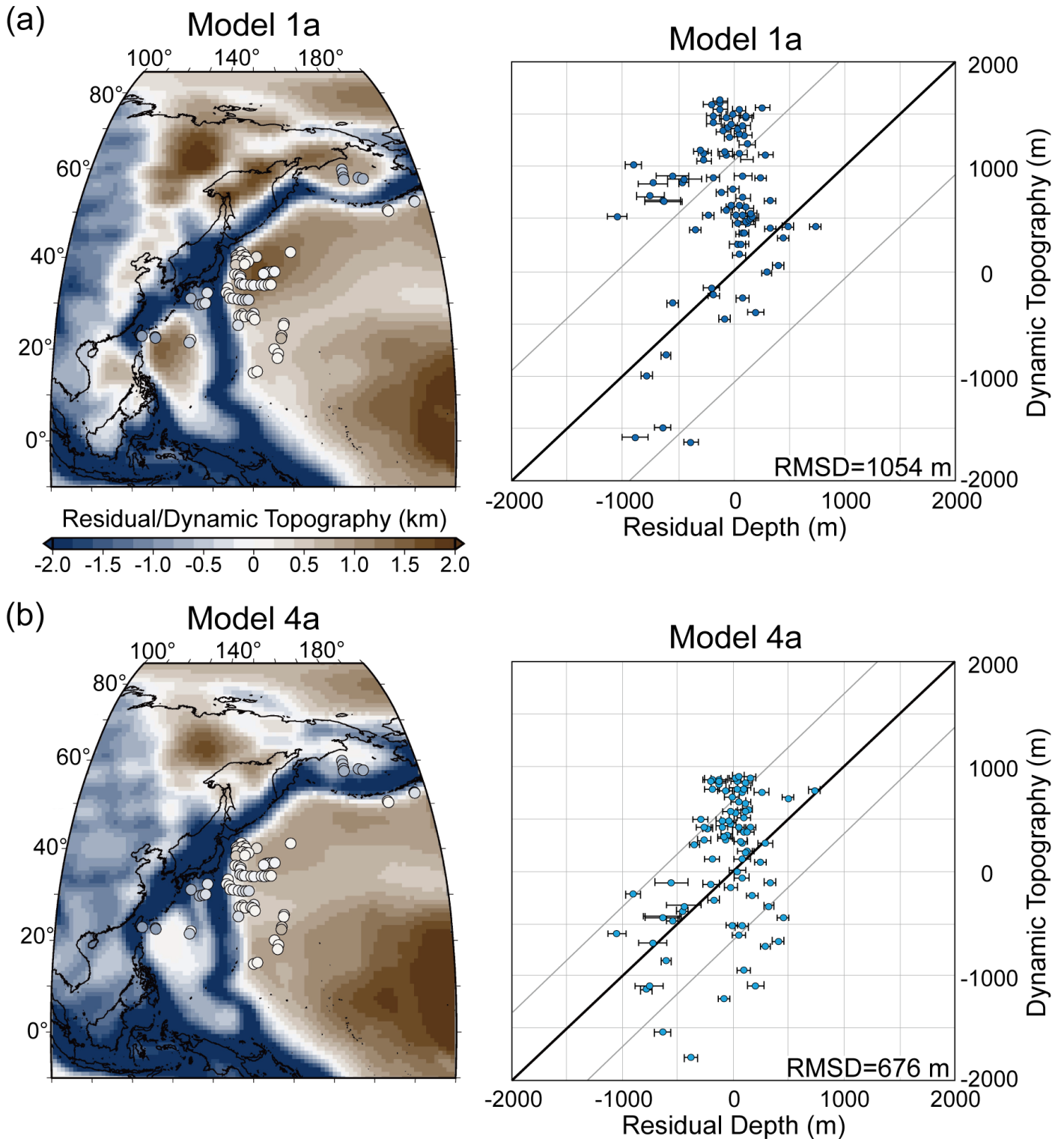
241

242 *3.3 Comparison of modeled dynamic topography and observed residual topography*

243

244 We focus here on the present-day dynamic topography predicted by our best-fit model
245 (viscosity profile 6 in Case a) and compare the results of the Andean-style Model 1a
246 and intra-oceanic Model 4a end-members (Fig. 5) against observed residual topography
247 (e.g. Hoggard et al., 2016). Global correlation between our predicted dynamic
248 topography and observed residual topography model (Hoggard et al., 2016) for degree
249 1-3 and is 0.49-0.56, which is comparable to a previous study (0.31-0.55) (Flament,
250 2018) indicating a reasonable result. Focusing on dynamic topography predictions in the
251 western Pacific, we show the present-day dynamic topography up to degree 160 and
252 compare it to 83 most accurate spot measurements of Hoggard et al. (2017) (Fig. 5).
253 The root-mean-square deviation (RMSD) between dynamic and residual topography is
254 1054 m for Model 1a and 676 m for Model 4a (Fig. 5), indicating that intra-oceanic
255 Model 4a produces a superior fit. In particular, the Andean-style Model 1a misfits can be
256 primarily traced to excess dynamic topography within the Pacific Ocean offshore Japan,
257 with less prominent misfit contributions within the central Philippine Sea plate and
258 Bering Sea. Comparison of all Models 1a to 4a show that the intra-oceanic Models 2a to
259 4a uniformly produce a 20-25% improved fit between dynamic and residual topography
260 within the western Pacific Ocean (Fig. S16).

261



262
 263
 264
 265
 266
 267

Figure 5. (a) and (b) show maps of the dynamic topography in western Pacific predicted from Model 1a and Model 4a using viscosity profile 6. Colored circles show 83 spot residual topography measurements from Hoggard et al. (2017). (c) and (d) show scatter plots between dynamic topography and the 83 spot residual topography measurements in a), b). Black line delineates a 1:1 correlation; grey lines bound 1 root-mean-square

268 deviation (RMSD). Intra-oceanic Model 4a shows a superior match to residual
269 topography (i.e. lower RMSD error) compared to Andean-style Model 1a.
270

271 **4. Discussion**

272

273 *4.1 Implications for intra-oceanic subduction within the NW Pacific Ocean basin*

274

275 Our geoid and dynamic topography comparisons robustly show that intra-oceanic
276 Reconstructions 2 to 4 produce better matches to the real Earth than the Andean-style
277 Reconstruction 1 (Figs. 4, 5). Within the intra-oceanic Reconstructions, our results seem
278 to show that our most complex reconstruction (Reconstruction 4) generally produces the
279 best fit to the geoid, but more work is necessary to discern specific plate reconstruction
280 details between Reconstructions 2 to 4. Our results suggest that at least some accreted
281 oceanic terranes along the NW Pacific margin (Fig. 1a) could have originated from
282 Pacific-Panthalassan or East Asian backarc intra-oceanic subduction zones, providing
283 alternative explanations for East Asian margin allochthonous terranes (e.g. Sakashima
284 et al., 2003). This affirms previous tomography-based plate reconstructions from better-
285 imaged areas of the NW Pacific Ocean that showed probable Pacific-Panthalassa intra-
286 oceanic subduction during Mesozoic times (van der Meer et al., 2012), which have
287 implications for global CO₂ level estimates since the Triassic (Van Der Meer et al.,
288 2014). Regardless, our conclusions present important challenges to the Andean-style
289 margin assumptions that are deeply embedded into almost all current East Asian plate
290 tectonic, geodynamic and geological studies (Cao et al., 2018; Müller et al., 2019; Wu et
291 al., 2019).

292

293 Despite successful tests of predicted and imaged mantle structure within other East
294 Asian regions (e.g. Lin et al., 2020; Seton et al., 2015), our test under the NW Pacific
295 Ocean (Fig. 3) was inconclusive. Considering the extreme contrasts in assimilated plate
296 reconstructions (Fig. 2), the inability to differentiate between end-member plate
297 reconstructions from mantle structure is noteworthy, and is partly due to the limited
298 resolution of tomographic images in the lower mantle. Future improvements in central
299 Pacific seismic tomography may help constrain alternative reconstructions. However,
300 one important complicating factor is the lateral advection of lower mantle slabs within
301 the central Pacific Ocean, which contributes to the similarity of modeled present-day
302 mantle states (Fig. 3). The lateral advection was produced in all four reconstructions
303 (Fig. 3) and challenges 'vertical slab sinking' simplifying assumptions that have been
304 used in some tomography-based slab-plate reconstructions of Pacific-Panthalassa (e.g.
305 Sigloch & Mihalynuk, 2013; van der Meer et al., 2012). Significant lateral advection of
306 slab material is present in previous models (Seton et al., 2015; Zehrović et al., 2016)
307 and slabs are advected SE-wards in all our models by around 2500 km in the lower
308 mantle (Figs. 3, S6-11). The amount of lateral advection of slab material depends on
309 choices of geodynamic modelling parameters. Steinberger et al. (2012) reports lateral
310 advection of only a few degrees, on average, whereas Wang et al. (2018) illustrate how
311 mantle upwellings can act as attractors of subducted slab material, even in the
312 presence of thermo-chemical piles. Therefore, caution is needed when tomographic
313 images are used for restoring the absolute positions of ancient subduction zones, as

314 different interpretative assumptions can imply different styles of convection in the
315 Earth's mantle.

316

317 Our comparison between predicted and imaged mantle structure within the central
318 Pacific Ocean, which was made more explicit than previous attempts by our P-wave
319 tomographic filtering (Fig. 3 right column), illustrates how tomography-led plate
320 reconstructions of some ocean basins will have limitations due to poorer resolution (Fig.
321 3). Such tomographic blind spots have also confounded past studies (e.g. van der Meer
322 et al., 2012). Here we show the advantage of employing an array of comparisons to
323 forward geodynamic models (i.e. the geoid and dynamic topography) when faced with
324 potentially ambiguous comparisons to mantle structure. This approach may be
325 important for studies of other large ocean basins, such as the Indian Ocean-Tethys (e.g.
326 Nerlich et al., 2016), where seismic source-receiver pairings may also not be optimal for
327 imaging mantle structure within ocean basin center.

328

329 **Acknowledgements**

330

331 We thank Jeremy Tsung-Jui Wu, Yiduo Liu, Spencer Fuston, Hayato Ueda, Gaku
332 Kimura, Ying Song, Kazu Okamoto, Maria Seton and Kasra Hosseini for valuable
333 discussion and support, Nathan Simmons and Thomas Chust for assistance and helpful
334 discussions on mineral physics and tomographic filtering, and the University of Houston
335 (UH) Center for Tectonics and Tomography for organizing scientific workshops. Yi-An
336 Lin and Jonny Wu are supported by U.S. National Science Foundation grant EAR-

337 1848327. Yi-An Lin, Jonny Wu, and Lorenzo Colli acknowledge funding from the State
338 of Texas Governor's University Research Initiative (GURI), the use of the UH Sabine
339 Clusters, the advanced support from the UH Research Computing Data Core and
340 Gocad software educational licenses from Emerson Paradigm. GPLates files and movies
341 of all plate reconstructions are provided in the Supplemental materials. The vtk file for
342 the modeled present-day mantle temperature and velocity field can be found at Texas
343 Data Repository (<https://doi.org/10.18738/T8/KEFMWZ>).

344

345

346

References

347

348 Akinin, V. V., & Miller, E. L. (2011). Evolution of calc-alkaline magmas of the Okhotsk-
349 Chukotka volcanic belt. *Petrology*, 19(3), 237-277.
350 doi:<https://doi.org/10.1134/S0869591111020020>

351

352 Alexeiev, D. V., Gaedicke, C., Tsukanov, N. V., & Freitag, R. (2006). Collision of the
353 Kronotskiy arc at the NE Eurasia margin and structural evolution of the Kamchatka-
354 Aleutian junction. *International Journal of Earth Sciences*, 95(6), 977-993.
doi:<https://doi.org/10.1007/s00531-006-0080-z>

355

356 Boschman, L. M., & van Hinsbergen, D. J. J. (2016). On the enigmatic birth of the
357 Pacific Plate within the Panthalassa Ocean. *Science Advances*, 2(7), e1600022.
doi:<https://doi.org/10.1126/sciadv.1600022>

358

359 Boyden, J. A., Müller, R. D., Gurnis, M., Torsvik, T. H., Clark, J. A., Turner, M., . . .
360 Cannon, J. S. (2011). Next-generation plate-tectonic reconstructions using GPLates. In
361 Baru, C. & Keller, G. R. (Eds.), *Geoinformatics: Cyberinfrastructure for the Solid Earth
Sciences* (pp. 95-114). Cambridge: Cambridge University Press.

362

363 Bunge, H.-P., & Grand, S. P. (2000). Mesozoic plate-motion history below the northeast
364 Pacific Ocean from seismic images of the subducted Farallon slab. *Nature*, 405, 337-
340. doi:<https://doi.org/10.1038/35012586>

- 365 Bunge, H.-P., Richards, M. A., Lithgow-Bertelloni, C., Baumgardner, J. R., Grand, S. P.,
366 & Romanowicz, B. A. (1998). Time Scales and Heterogeneous Structure in Geodynamic
367 Earth Models. *Science*, 280(5360), 91-95.
368 doi:<https://doi.org/10.1126/science.280.5360.91>
- 369 Cai, G., Wan, Z., Yao, Y., Zhong, L., Zheng, H., Kapsiotis, A., & Zhang, C. (2019).
370 Mesozoic Northward Subduction Along the SE Asian Continental Margin Inferred from
371 Magmatic Records in the South China Sea. *Minerals*, 9(10).
372 doi:<https://doi.org/10.3390/min9100598>
- 373 Cao, X., Flament, N., Müller, D., & Li, S. (2018). The Dynamic Topography of Eastern
374 China Since the Latest Jurassic Period. *Tectonics*, 37(5), 1274-1291.
375 doi:<https://doi.org/10.1029/2017TC004830>
- 376 Chust, T. C., Steinle-Neumann, G., Dolejš, D., Schuberth, B. S. A., & Bunge, H. P.
377 (2017). MMA-EoS: A Computational Framework for Mineralogical Thermodynamics.
378 *Journal of Geophysical Research: Solid Earth*, 122(12), 9881-9920.
379 doi:<https://doi.org/10.1002/2017JB014501>
- 380 Domeier, M., Shephard, G. E., Jakob, J., Gaina, C., Doubrovine, P. V., & Torsvik, T. H.
381 (2017). Intraoceanic subduction spanned the Pacific in the Late Cretaceous–Paleocene.
382 *Science Advances*, 3(11), eaao2303.
383 doi:<https://doi.org/10.1038/ngeo111110.1126/sciadv.aao2303>
- 384 Dong, S., Zhang, Y., Li, H., Shi, W., Xue, H., Li, J., . . . Wang, Y. (2018). The Yanshan
385 orogeny and late Mesozoic multi-plate convergence in East Asia—Commemorating
386 90th years of the “Yanshan Orogeny”. *Science China Earth Sciences*, 61, 1888-1909.
387 doi:<https://doi.org/10.1038/ngeo111110.1007/s11430-017-9297-y>
- 388 Engebretson, D. C., Cox, A., & Gordon, R. G. (1984). Relative motions between oceanic
389 plates of the Pacific Basin. *Journal of Geophysical Research: Solid Earth*, 89(B12),
390 10291-10310. doi:<https://doi.org/10.1038/ngeo111110.1130/SPE206-p1>
- 391 Filatova, N. I., & Vishnevskaya, V. S. (1997). Radiolarian stratigraphy and origin of the
392 Mesozoic terranes of the continental framework of the northwestern Pacific (Russia).
393 *Tectonophysics*, 269(1), 131-150. doi:[https://doi.org/10.1016/S0040-1951\(96\)00156-4](https://doi.org/10.1016/S0040-1951(96)00156-4)
- 394 Flament, N. (2018). Present-day dynamic topography and lower-mantle structure from
395 palaeogeographically constrained mantle flow models. *Geophysical Journal
396 International*, 216(3), 2158-2182.
397 doi:<https://doi.org/10.1038/ngeo111110.1093/gji/ggy526>

398 Fujisaki, W., Isozaki, Y., Maki, K., Sakata, S., Hirata, T., & Maruyama, S. (2014). Age
399 spectra of detrital zircon of the Jurassic clastic rocks of the Mino-Tanba AC belt in SW
400 Japan: Constraints to the provenance of the mid-Mesozoic trench in East Asia. *Journal*
401 *of Asian Earth Sciences*, 88, 62-73. doi:<https://doi.org/10.1016/j.jseaes.2014.02.006>

402 Gurnis, M., Turner, M., Zahirovic, S., DiCaprio, L., Spasojevic, S., Müller, R. D., . . .
403 Bower, D. J. (2012). Plate tectonic reconstructions with continuously closing plates.
404 *Computers & Geosciences*, 38(1), 35-42. doi:10.1016/j.cageo.2011.04.014

405 Hager, B. H., Richards, M. A., apos, Nions, R. K., Clayton, R., & Parsons, B. (1989).
406 Long-wavelength variations in Earth's geoid: physical models and dynamical
407 implications. *Philosophical Transactions of the Royal Society of London. Series A,*
408 *Mathematical and Physical Sciences*, 328(1599), 309-327. doi:10.1098/rsta.1989.0038

409 Hoggard, M. J., White, N., & Al-Attar, D. (2016). Global dynamic topography
410 observations reveal limited influence of large-scale mantle flow. *Nature Geoscience*, 9,
411 456–463. doi:<https://doi.org/10.1038/ngeo2709>

412 Hoggard, M. J., Winterbourne, J., Czarnota, K., & White, N. (2017). Oceanic residual
413 depth measurements, the plate cooling model, and global dynamic topography. *Journal*
414 *of Geophysical Research: Solid Earth*, 122(3), 2328-2372.
415 doi:<https://doi.org/10.1002/2016JB013457>

416 Hosseini, K., Sigloch, K., Tsekhmistrenko, M., Zaheri, A., Nissen-Meyer, T., & Igel, H.
417 (2020). Global mantle structure from multifrequency tomography using P, PP and P-
418 diffracted waves. *Geophysical Journal International*, 220(1), 96-141.
419 doi:10.1093/gji/ggz394

420 Hourigan, J. K., & Akinin, V. V. (2004). Tectonic and chronostratigraphic implications of
421 new ⁴⁰Ar/³⁹Ar geochronology and geochemistry of the Arman and Malan-Ola volcanic
422 fields, Okhotsk-Chukotka volcanic belt, northeastern Russia. *GSA Bulletin*, 116(5-6),
423 637-654. doi:10.1130/B25340.1

424 Jarvis, G. T., & McKenzie, D. P. (1980). Convection in a compressible fluid with infinite
425 Prandtl number. *Journal of Fluid Mechanics*, 96(3), 515-583.
426 doi:<https://doi.org/10.1017/S002211208000225X>

427 Keating, B. H., Matthey, D. P., Helsley, C. E., Naughton, J. J., Epp, D., Lazarewicz, A., &
428 Schwank, D. (1984). Evidence for a hot spot origin of the Caroline Islands. *Journal of*
429 *Geophysical Research: Solid Earth*, 89(B12), 9937-9948.
430 doi:<https://doi.org/10.1029/JB089iB12p09937>

- 431 Konstantinovskaia, E. A. (2000). Geodynamics of an Early Eocene arc–continent
432 collision reconstructed from the Kamchatka Orogenic Belt, NE Russia. *Tectonophysics*,
433 325(1), 87-105. doi:[https://doi.org/10.1016/S0040-1951\(00\)00132-3](https://doi.org/10.1016/S0040-1951(00)00132-3)
- 434 Li, C., van der Hilst, R. D., Engdahl, E. R., & Burdick, S. (2008). A new global model
435 for P-wave speed variations in Earth's mantle. *Geochemistry, Geophysics, Geosystems*,
436 9(5), Q0501. doi:<https://doi.org/10.1029/2007gc001806>
- 437 Lin, Y.-A., Colli, L., Wu, J., & Schuberth, B. S. A. (2020). Where Are the Proto-South
438 China Sea Slabs? SE Asian Plate Tectonics and Mantle Flow History From Global
439 Mantle Convection Modeling. *Journal of Geophysical Research: Solid Earth*, 125(12),
440 e2020JB019758. doi:<https://doi.org/10.1029/2020JB019758>
- 441 Matthews, K. J., Maloney, K. T., Zahirovic, S., Williams, S. E., Seton, M., & Müller, R. D.
442 (2016). Global plate boundary evolution and kinematics since the late Paleozoic. *Global
443 and Planetary Change*, 146, 226-250.
444 doi:<https://doi.org/10.1016/j.gloplacha.2016.10.002>
- 445 Müller, R. D., Seton, M., Zahirovic, S., Williams, S. E., Matthews, K. J., Wright, N.
446 M., . . . Cannon, J. (2016). Ocean Basin Evolution and Global-Scale Plate
447 Reorganization Events Since Pangea Breakup. *Annual Review of Earth and Planetary
448 Sciences*, 44(1), 107-138. doi:<https://doi.org/10.1146/annurev-earth-060115-012211>
- 449 Müller, R. D., Zahirovic, S., Williams, S. E., Cannon, J., Seton, M., Bower, D. J., . . .
450 Gurnis, M. (2019). A global plate model including lithospheric deformation along major
451 rifts and orogens since the Triassic. *Tectonics*, 38, 1884–1907.
452 doi:<https://doi.org/10.1029/2018TC005462>
- 453 Nerlich, R., Colli, L., Ghelichkhan, S., Schuberth, B., & Bunge, H.-P. (2016).
454 Constraining central Neo-Tethys Ocean reconstructions with mantle convection models.
455 *Geophysical Research Letters*, 43(18), 9595-9603.
456 doi:<https://doi.org/10.1002/2016GL070524>
- 457 Nokleberg, W. J., (Eds). (2010). *Metallogenesis and Tectonics of Northeast Asia: U.S
458 Geological Survey Professional Paper 1765*, 624p. Reston, Virginia: U.S Geological
459 Survey.
- 460 Obayashi, M., Yoshimitsu, J., Nolet, G., Fukao, Y., Shiobara, H., Sugioka, H., . . . Gao,
461 Y. (2013). Finite frequency whole mantle P-wave tomography: Improvement of subducted
462 slab images. *Geophysical Research Letters*, 40(21), 5652-5657.
463 doi:<https://doi.org/10.1002/2013gl057401>

- 464 Pail, R., Bruinsma, S., Migliaccio, F., Förste, C., Goiginger, H., Schuh, W.-D., . . .
465 Tscherning, C. C. (2011). First GOCE gravity field models derived by three different
466 approaches. *Journal of Geodesy*, 85(11), 819. doi:10.1007/s00190-011-0467-x
- 467 Pekeris, C. L. (1935). Thermal Convection in the Interior of the Earth. *Geophysical*
468 *Supplements to the Monthly Notices of the Royal Astronomical Society*, 3(8), 343-367.
469 doi:10.1111/j.1365-246X.1935.tb01742.x
- 470 Ritsema, J., Deuss, A., van Heijst, H. J., & Woodhouse, J. H. (2011). S40RTS: a
471 degree-40 shear-velocity model for the mantle from new Rayleigh wave dispersion,
472 teleseismic traveltimes and normal-mode splitting function measurements. *Geophysical*
473 *Journal International*, 184(3), 1223-1236. doi:[https://doi.org/10.1111/j.1365-](https://doi.org/10.1111/j.1365-246X.2010.04884.x)
474 [246X.2010.04884.x](https://doi.org/10.1111/j.1365-246X.2010.04884.x)
- 475 Sakashima, T., Terada, K., Takeshita, T., & Sano, Y. (2003). Large-scale displacement
476 along the Median Tectonic Line, Japan: evidence from SHRIMP zircon U–Pb dating of
477 granites and gneisses from the South Kitakami and paleo-Ryoke belts. *Journal of Asian*
478 *Earth Sciences*, 21(9), 1019-1039. doi:[https://doi.org/10.1016/S1367-9120\(02\)00108-6](https://doi.org/10.1016/S1367-9120(02)00108-6)
- 479 Schuberth, B. S. A., Bunge, H. P., & Ritsema, J. (2009). Tomographic filtering of high-
480 resolution mantle circulation models: Can seismic heterogeneity be explained by
481 temperature alone? *Geochemistry, Geophysics, Geosystems*, 10(5), Q05W03.
482 doi:<https://doi.org/10.1029/2009GC002401>
- 483 Seton, M., Flament, N., & Whittaker, J. (2018). *Geodynamic history of subducted slabs*
484 *along the East Asian margin since the Cretaceous*. Paper presented at the Japan
485 Geoscience Union Meeting 2018, Tokyo, Japan.
- 486 Seton, M., Flament, N., Whittaker, J., Müller, R. D., Gurnis, M., & Bower, D. J. (2015).
487 Ridge subduction sparked reorganization of the Pacific plate-mantle system 60–50
488 million years ago. *Geophysical Research Letters*, 42(6), 1732-1740.
489 doi:<https://doi.org/10.1002/2015GL063057>
- 490 Seton, M., Müller, R. D., Zahirovic, S., Gaina, C., Torsvik, T., Shephard, G., . . .
491 Chandler, M. (2012). Global continental and ocean basin reconstructions since 200Ma.
492 *Earth-Science Reviews*, 113(3), 212-270.
493 doi:<https://doi.org/10.1016/j.earscirev.2012.03.002>
- 494 Shapiro, M. N., & Solov'ev, A. V. (2009). Formation of the Olyutorsky–Kamchatka
495 foldbelt: a kinematic model. *Russian Geology and Geophysics*, 50(8), 668-681.
496 doi:<https://doi.org/10.1016/j.rgg.2008.10.006>

- 497 Sigloch, K., & Mihalynuk, M. G. (2013). Intra-oceanic subduction shaped the assembly
498 of Cordilleran North America. *Nature*, 496(7443), 50–56.
499 doi:<https://doi.org/10.1038/nature12019>
- 500 Simmons, N. A., Myers, S. C., Johannesson, G., Matzel, E., & Grand, S. P. (2015).
501 Evidence for long-lived subduction of an ancient tectonic plate beneath the southern
502 Indian Ocean. *Geophysical Research Letters*, 42(21), 9270-9278.
503 doi:<https://doi.org/10.1002/2015GL066237>
- 504 Simmons, N. A., Schuberth, B. S. A., Myers, S. C., & Knapp, D. R. (2019). Resolution
505 and Covariance of the LLNL-G3D-JPS Global Seismic Tomography Model: Applications
506 to Travel time Uncertainty and Tomographic Filtering of Geodynamic Models.
507 *Geophysical Journal International*, 217(3), 1543-1557.
508 doi:<https://doi.org/10.1093/gji/ggz102>
- 509 Steinberger, B., & Calderwood, A. R. (2006). Models of large-scale viscous flow in the
510 Earth's mantle with constraints from mineral physics and surface observations.
511 *Geophysical Journal International*, 167(3), 1461-1481.
512 doi:<https://doi.org/10.1111/j.1365-246X.2006.03131.x>
- 513 Steinberger, B., & Holme, R. (2008). Mantle flow models with core-mantle boundary
514 constraints and chemical heterogeneities in the lowermost mantle. *Journal of*
515 *Geophysical Research: Solid Earth*, 113(B5), B05403.
516 doi:<https://doi.org/10.1029/2007JB005080>
- 517 Steinberger, B., Torsvik, T. H., & Becker, T. W. (2012). Subduction to the lower mantle
518 – a comparison between geodynamic and tomographic models. *Solid Earth*, 3(2),
519 415-432. doi:10.5194/se-3-415-2012
- 520 Stixrude, L., & Lithgow-Bertelloni, C. (2011). Thermodynamics of mantle minerals – II.
521 Phase equilibria. *Geophysical Journal International*, 184(3), 1180-1213.
522 doi:<https://doi.org/10.1111/j.1365-246X.2010.04890.x>
- 523 Thoraval, C., & Richards, M. A. (1997). The geoid constraint in global geodynamics:
524 viscosity structure, mantle heterogeneity models and boundary conditions. *Geophysical*
525 *Journal International*, 131(1), 1-8. doi:10.1111/j.1365-246X.1997.tb00591.x
- 526 Torsvik, T. H., Steinberger, B., Shephard, G. E., Doubrovine, P. V., Gaina, C., Domeier,
527 M., . . . Sager, W. W. (2019). Pacific-Panthalassic Reconstructions: Overview, Errata
528 and the Way Forward. *Geochemistry, Geophysics, Geosystems*, 20(7), 3659-3689.
529 doi:10.1029/2019GC008402

- 530 Ueda, H., & Miyashita, S. (2005). Tectonic accretion of a subducted intraoceanic
531 remnant arc in Cretaceous Hokkaido, Japan, and implications for evolution of the Pacific
532 northwest. *The Island Arc*, 14, 582–598. doi:[https://doi.org/10.1111/j.1440-
533 1738.2005.00486.x](https://doi.org/10.1111/j.1440-1738.2005.00486.x)
- 534 Vaes, B., van Hinsbergen, D. J. J., & Boschman, L. M. (2019). Reconstruction of
535 Subduction and Back-Arc Spreading in the NW Pacific and Aleutian Basin: Clues to
536 Causes of Cretaceous and Eocene Plate Reorganizations. *Tectonics*, 38(4), 1367-1413.
537 doi:<https://doi.org/10.1029/2018TC005164>
- 538 van der Meer, D. G., Torsvik, T. H., Spakman, W., van Hinsbergen, D. J. J., & Amaru,
539 M. L. (2012). Intra-Panthalassa Ocean subduction zones revealed by fossil arcs and
540 mantle structure. *Nature Geoscience*, 5(3), 215-219.
541 doi:<https://doi.org/10.1038/ngeo1401>
- 542 Van Der Meer, D. G., Zeebe, R. E., van Hinsbergen, D. J. J., Sluijs, A., Spakman, W., &
543 Torsvik, T. H. (2014). Plate tectonic controls on atmospheric CO₂ levels since the Triassic. *Proceedings of the National Academy of Sciences*, 111(12),
544 4380. doi:10.1073/pnas.1315657111
- 546 Wang, H., Wang, Y., Gurnis, M., Zahirovic, S., & Leng, W. (2018). A long-lived Indian
547 Ocean slab: Deep dip reversal induced by the African LLSVP. *Earth and Planetary
548 Science Letters*, 497, 1-11. doi:<https://doi.org/10.1016/j.epsl.2018.05.050>
- 549 Whittaker, J. M., Müller, R. D., Leitchenkov, G., Stagg, H., Sdrolias, M., Gaina, C., &
550 Goncharov, A. (2007). Major Australian-Antarctic Plate Reorganization at Hawaiian-
551 Emperor Bend Time. *Science*, 318(5847), 83-86.
552 doi:<https://doi.org/10.1126/science.1143769>
- 553 Wright, N. M., Seton, M., Williams, S. E., & Müller, R. D. (2016). The Late Cretaceous to
554 recent tectonic history of the Pacific Ocean basin. *Earth-Science Reviews*, 154, 138-
555 173. doi:<https://doi.org/10.1016/j.earscirev.2015.11.015>
- 556 Wu, F.-Y., Yang, J.-H., Xu, Y.-G., Wilde, S. A., & Walker, R. J. (2019). Destruction of
557 the North China Craton in the Mesozoic. *Annual Review of Earth and Planetary
558 Sciences*, 47(1), 173-195. doi:<https://doi.org/10.1146/annurev-earth-053018-060342>
- 559 Wu, J., Suppe, J., Lu, R., & Kanda, R. (2016). Philippine Sea and East Asian plate
560 tectonics since 52 Ma constrained by new subducted slab reconstruction methods.
561 *Journal of Geophysical Research: Solid Earth*, 121(6), 4670-4741.
562 doi:<https://doi.org/10.1002/2016JB012923>

- 563 Wu, T.-J. J., & Wu, J. (2019). Izanagi-Pacific ridge subduction revealed by a 56 to 46
564 Ma magmatic gap along the northeast Asian margin. *Geology*, 47(10), 953-957.
565 doi:<https://doi.org/10.1130/G46778.1>
- 566 Xinmin, Z., Tao, S., Weizhou, S., Liangshu, S., & Niu, Y. (2006). Petrogenesis of
567 Mesozoic granitoids and volcanic rocks in South China: A response to tectonic
568 evolution. *International Union of Geological Sciences*, 29(1), 26-33.
569 doi:<https://doi.org/10.18814/epiiugs/2006/v29i1/004>
- 570 Yamasaki, T., & Nanayama, F. (2018). Immature intra-oceanic arc-type volcanism on
571 the Izanagi Plate revealed by the geochemistry of the Daimaruyama greenstones in the
572 Hiroo Complex, southern Hidaka Belt, central Hokkaido, Japan. *Lithos*, 302-303, 224-
573 241. doi:<https://doi.org/10.1016/j.lithos.2018.01.003>
- 574 Zahirovic, S., Matthews, K. J., Flament, N., Müller, R. D., Hill, K. C., Seton, M., &
575 Gurnis, M. (2016). Tectonic evolution and deep mantle structure of the eastern Tethys
576 since the latest Jurassic. *Earth-Science Reviews*, 162, 293-337.
577 doi:<https://doi.org/10.1016/j.earscirev.2016.09.005>
- 578 Zharov, A. E. (2005). South Sakhalin tectonics and geodynamics: A model for the
579 Cretaceous-Paleogene accretion of the East Asian continental margin. *Russian Journal
580 of Earth Sciences*, 7, ES5002.
- 581 Zhou, X. M., & Li, W. X. (2000). Origin of Late Mesozoic igneous rocks in Southeastern
582 China: implications for lithosphere subduction and underplating of mafic magmas.
583 *Tectonophysics*, 326(3), 269-287. doi:[https://doi.org/10.1016/S0040-1951\(00\)00120-7](https://doi.org/10.1016/S0040-1951(00)00120-7)
584